

SPADE4: Sparsity and Delay Embedding based Forecasting of Epidemics

Esha Saha^{*1}, Lam Si Tung Ho², and Giang Tran¹

¹Department of Applied Mathematics, University of Waterloo

²Department of Mathematics and Statistics, Dalhousie University

Abstract

Predicting the evolution of diseases is challenging, especially when the data availability is scarce and incomplete. The most popular tools for modelling and predicting infectious disease epidemics are compartmental models. They stratify the population into compartments according to health status and model the dynamics of these compartments using dynamical systems. However, these predefined systems may not capture the true dynamics of the epidemic due to the complexity of the disease transmission and human interactions. In order to overcome this drawback, we propose **Sparsity** and **Delay Embedding** based **Forecasting** (SPADE4) for predicting epidemics. SPADE4 predicts the future trajectory of an observable variable without the knowledge of the other variables or the underlying system. We use random features model with sparse regression to handle the data scarcity issue and employ Takens' delay embedding theorem to capture the nature of the underlying system from the observed variable. We show that our approach outperforms compartmental models when applied to both simulated and real data.

Keywords: sparse regression, random feature models, infectious diseases, delay embedding

1 Introduction

Humans and pathogens have always been in a race to beat each other. Whenever the human community is introduced to new diseases, people either control the spread through various measures or gain immunity through infection, medications and/or vaccinations. However, when a disease is new to the community, there is a need to understand, analyze and predict its evolution so that at a social level, spread of the disease can be managed and enough information regarding the disease causing pathogen can be made available for scientists to come up with medications and/or vaccinations. Numerous works have been trying to study the nature of epidemics using mathematical techniques in epidemiology and/or machine learning.

Surveillance data, such as daily cases, are the prime source of information about emerging infectious disease epidemics. Predicting the trajectories of epidemics from surveillance data is currently one of the most active research areas, partially due to the COVID-19 pandemic. Compartmental models, which stratify the population into compartments according to health status, are the most

^{*}The code is available at <https://github.com/esha-saha/spade4>.

popular tools for this task. They have been used to study many infectious disease epidemics including plague [16], Ebola [1, 15], measles [8], HIV [4], influenza [11], and COVID-19 [54, 10]. These models utilize dynamical systems to describe the dynamics of their compartments.

For example, the classic Susceptible-Exposed-Infectious-Recovered (SEIR) divide the population into four groups: Susceptible (healthy), Exposed (infected but not yet infectious), Infectious (infected and infectious), and Recovered (recovered or died). Let S, E, I, R be the population of Susceptible, Exposed, Infected, Recovered groups respectively. Under the SEIR model, we have

$$\begin{aligned}\frac{dS}{dt} &= -\frac{\beta SI}{P} \\ \frac{dE}{dt} &= \frac{\beta SI}{P} - \sigma E \\ \frac{dI}{dt} &= \sigma E - \gamma I \\ \frac{dR}{dt} &= \gamma I,\end{aligned}\tag{1}$$

where β is infection rate, σ is the latency rate, γ is the removal rate and P denotes the population. By learning these parameters from surveillance data, one can predict the future trajectories of the epidemic. However, the SEIR model is often too simple to fully capture the dynamics of an epidemic. Therefore, much effort has been made to modify the SEIR model according to the nature of the infectious disease. One such model is the $S\mu$ SEIR model described in [54] which takes into account unreported cases. The dynamics of this model is given by

$$\begin{aligned}\frac{dS}{dt} &= -\frac{\beta(I + E)S}{P} \\ \frac{dE}{dt} &= \frac{\beta(I + E)S}{P} - \sigma E \\ \frac{dI}{dt} &= \mu\sigma E - \gamma I \\ \frac{dR}{dt} &= \gamma I,\end{aligned}\tag{2}$$

where the parameter μ represents the rate of unreported cases. Nevertheless, the performance of compartmental models depends heavily on how well the predefined dynamical system can capture the dynamic of an epidemic. In this paper, we propose a machine learning method for predicting infectious disease epidemics. Unlike compartmental models, our approach does not make any assumption on the underlying dynamical system.

Typical machine learning or artificial intelligence based methods aim to learn the trajectory of a dynamical system from a d -dimensional time dependent data $\mathbf{x}(t) \in \mathbb{R}^d$ by finding a function f such that $\frac{d\mathbf{x}(t)}{dt} = f(\mathbf{x}(t))$. This comes under an active area of research involving learning of dynamical systems from data. One class of methods assumes the underlying dynamical system to have sparse representations with respect to a prescribed dictionary consisting of polynomials and/or trigonometric functions. Sparse regression is used to identify these active terms [20, 29, 7, 40, 47, 43, 42, 13]. Another approach based on neural networks is modeling partial or ordinary differential equations using either full data or partial observations with some side information to learn the system [50, 30, 2, 36, 12, 22, 44, 27, 28, 32, 45, 49]. Other works in [26, 24, 3] demonstrate the power

of using deep learning for approximating operators between functional spaces. However, neural networks perform well only when they have enough training data. This makes their applications limited in the data scarce regime. Another issue with neural networks is the lack of its theoretical understanding owing to its complexity. Random feature models proposed in [33, 34, 35] provide an alternative to using neural networks without compromising on the accuracy. Results in [18, 53, 51] demonstrate that it is possible to gain theoretical understanding of random feature models. These class of methods have also been successfully used in [31] for learning operators between Banach spaces. Sparse Random Feature Extraction proposed in [14] modifies random feature models to make it more suitable for data scarce problems by incorporating sparsity in building of the feature space. Similar works on sparse random feature models and feature selection using different methods have been widely explored in [41, 37, 52]. Most of those methods rely on the assumption that full state information is available. However, epidemiological data are often only partially observed where available observations are either daily active cases or cumulative cases. Therefore, the machine learning methods mentioned above are not applicable for learning the dynamics of the epidemics. Motivated by various delay embedding theorems such as the Whitney embedding theorem and Takens' theorem [46], we employ the delayed embedding method in our epidemiological forecast model. Delay embedding has been used to develop eigensystem realization algorithm in system identification to learn the eigensystem [19], to extract qualitative dynamics from data [5], and to study nonlinear dynamics in the Koopman operator framework [23, 6, 9, 21]. Delay embedding can be combined with neural networks to identify parameters and make prediction [25, 48]. It is worth noting that Takens' embedding theorem identify the model up to a diffeomorphism. Therefore, learning the original dynamical system from partially observed using delay embedding remains open.

In our work, we illustrate that it is feasible to forecast future dynamics of infectious disease epidemics using delay embedding. Specifically, we approximate the rate of change in the observed variable (daily active or cumulative cases) as a sparse random feature expansion of its time delayed mapping. Here, a sparsity constraint in the random feature model help balance between the richness representation of the function space and the limited amount of available data. Then, we use the learned function to make a prediction over a future time window. The proposed procedure is called Sparsity and Delay Embedding based Forecasting (SPADE4). We test SPADE4 on simulated data and consider cases where the input is without or with noise, and also test with different levels of noise. We show that SPADE4 performs consistently well over the SEIR and $S\mu$ EIR models on simulated data. Moreover, SPADE4 outperforms these models in predicting future trajectories of various epidemics including COVID-19 in Canada, Ebola in Guinea, Zika in Giradot and Flu in China.

2 Motivation and Problem Setting

Throughout the paper, we use bold letters for column vectors (e.g. \mathbf{x}) and bold capital letters for matrices (e.g. \mathbf{A}). A dot above a variable denotes time differentiation (e.g. $\dot{y}(t)$). We say that a vector \mathbf{z} is s -sparse if it has at most s nonzero entries. Let $[N]$ denote the set of all positive integers less than or equal to N . We denote the ℓ^p -norm of a vector \mathbf{z} by $\|\mathbf{z}\|_p$.

Given time-dependent observations $\{y(t_k)\}_{k=1}^m$ from an unknown multidimensional dynamical system, we propose a new inference method motivated by Takens' Theorem where we aim to forecast the values of $y(t)$ over a given forecast horizon (generally one-week-ahead forecast). First proposed

in 1981 in [46], given a dynamical system $\varphi : M \rightarrow M$, (M is a compact manifold of dimension d) and an observable $y : M \rightarrow \mathbb{R}$, Takens' theorem aims to obtain information about the original dynamical system. We recall the formal statement of Takens' Theorem as stated in [46, 17].

Theorem 2.1 (Takens' Theorem). . *Let M be a compact manifold of dimension d . For pairs (φ, y) , with $\varphi : M \rightarrow M$ a smooth diffeomorphism and $y : M \rightarrow \mathbb{R}$ a smooth function, it is generic property that the map $\Phi_{(\varphi, y)} : M \rightarrow \mathbb{R}^{2d+1}$, defined by*

$$\Phi_{(\varphi, y)}(\mathbf{x}) = (y(\mathbf{x}), y(\varphi(\mathbf{x})), \dots, y(\varphi^{2d}(\mathbf{x}))) \quad (3)$$

is an embedding.

The term 'generic' here means open and dense and by "smooth" we mean at least twice continuously differentiable and the function Φ is called the time delay mapping.

Motivated by Takens' theorem, we assume that the rate of change in the observable $y(t)$ is a function of its time delayed mapping Φ , i.e.,

$$\dot{y}(t_k) = f(y(t_k), y(t_{k-1}), \dots, y(t_{k-(p-1)})), \quad (4)$$

where p is the embedding dimension. We wish to learn the function $f : \mathbb{R}^p \rightarrow \mathbb{R}$ of the form

$$f(\mathbf{h}) \approx \sum_{j=1}^N c_j \phi(\langle \mathbf{h}, \boldsymbol{\omega}_j \rangle), \quad (5)$$

where $\mathbf{h}, \boldsymbol{\omega}_j \in \mathbb{R}^p$, $\boldsymbol{\omega}_j$ are the random weights, ϕ is a nonlinear activation function and $\mathbf{c} = [c_1 \dots c_N]^T \in \mathbb{R}^N$ is the trainable coefficient vector. The nonlinear activation function $\phi : \mathbb{R} \rightarrow \mathbb{R}$ can be chosen to be a trigonometric function, the sigmoid function, or the ReLU function. Here, we use the ReLU activation function, i.e. $\phi(\cdot) = \max\{0, \cdot\}$. Entries of the random weight vector are i.i.d. random variables generated by a probability function $\rho(\omega)$, while the coefficients $\mathbf{c} \in \mathbb{R}^N$ are trainable. Also known as random features model proposed in [33, 34, 35], this model can be considered as a wide two-layer neural network where the weights in the first hidden layer is generated (following a distribution) and frozen while training problem relies on learning the coefficient vector \mathbf{c} . Since we assume limited data availability, we wish to have a sparse representation of the function f by learning the coefficient vector \mathbf{c} with a sparsity constraint. Theoretically, when N is very large, the random feature methods has been shown to be comparable with shallow networks in terms of theoretical risk bounds [33, 35, 34, 39].

Given m measurements of the observable y , we first build the input-output pairs $\{(\mathbf{h}_k, \dot{y}(t_k))\}_{k=p}^m$, where $\mathbf{h}_k = [y(t_k), y(t_{k-1}), \dots, y(t_{k-p+1})]^T$ for $k = p, p+1, \dots, m$. We approximate the output data $\{\dot{y}(t_k)\}_{k=1}^m$ from given input data $\{y(t_k)\}_{k=1}^m$ using finite difference methods. In all our numerical simulations, we build the output data as follows:

$$\dot{y}(t_1) = \frac{y(t_2) - y(t_1)}{(t_2 - t_1)}; \dot{y}(t_k) = \frac{y(t_{k+1}) - y(t_{k-1})}{(t_{k+1} - t_{k-1})} \text{ for } k = 2, \dots, m-1; \dot{y}(t_m) = \frac{y(t_m) - y(t_{m-1})}{(t_m - t_{m-1})}. \quad (6)$$

If the data is noisy, then an additional step would be required after getting the output data since finite difference methods may amplify the noise in the input dataset making recovery difficult.

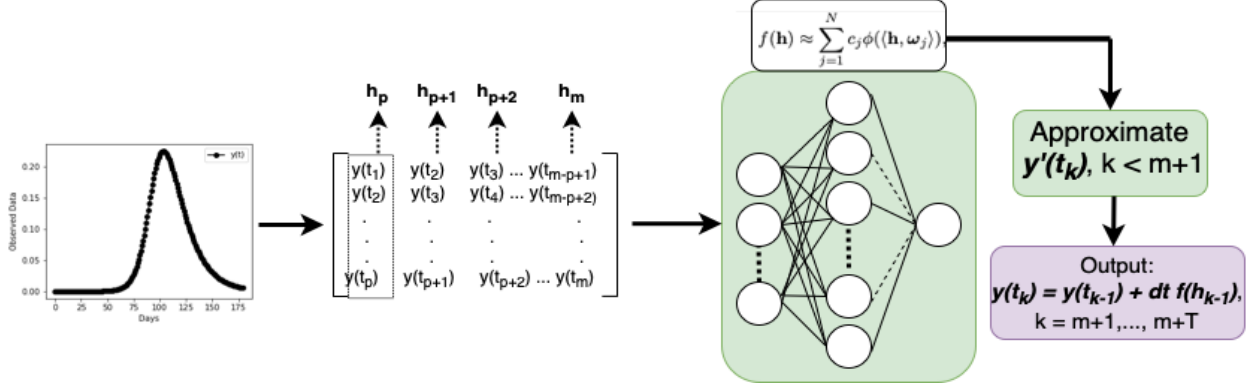


Figure 1: Schematic representation of SPADE4 algorithm.

We apply a convolution based averaging filter on $\{\dot{y}(t_k)\}_{k=1}^m$ with a smoothing parameter s as given below,

$$\dot{y}(t_k) = \frac{1}{s} \sum_{n=(k+1)-(s-1)}^{k+1} \dot{y}(t_n) \quad (7)$$

where $\dot{y}(t_k) = 0 \forall k \leq 0$ and $k \geq m+1$ and s denotes the strength of the smoothing filter. The value of s chosen is dependent upon the noise level present in the dataset. The value of s used for each of the experiments have been specified in their respective sections. Let $\mathbf{z} = [\dot{y}(t_p), \dot{y}(t_{p+1}), \dots, \dot{y}(t_m)]^T$ and $\mathbf{A} = (\phi(\langle \mathbf{h}_k, \omega_j \rangle)) \in \mathbb{R}^{(m-p+1) \times N}$. The matrix \mathbf{A} is given by,

$$\mathbf{A} = \begin{bmatrix} \phi(\langle \mathbf{h}_p, \omega_1 \rangle) & \phi(\langle \mathbf{h}_p, \omega_2 \rangle) & \phi(\langle \mathbf{h}_p, \omega_3 \rangle) & \dots & \phi(\langle \mathbf{h}_p, \omega_N \rangle) \\ \phi(\langle \mathbf{h}_{p+1}, \omega_1 \rangle) & \phi(\langle \mathbf{h}_{p+1}, \omega_2 \rangle) & \phi(\langle \mathbf{h}_{p+1}, \omega_3 \rangle) & \dots & \phi(\langle \mathbf{h}_{p+1}, \omega_N \rangle) \\ \vdots & \vdots & \vdots & \vdots & \vdots \\ \phi(\langle \mathbf{h}_m, \omega_1 \rangle) & \phi(\langle \mathbf{h}_m, \omega_2 \rangle) & \phi(\langle \mathbf{h}_m, \omega_3 \rangle) & \dots & \phi(\langle \mathbf{h}_m, \omega_N \rangle) \end{bmatrix} \in \mathbb{R}^{(m-p+1) \times N} \quad (8)$$

The problem (5) becomes,

$$\text{find } \mathbf{c} \in \mathbb{R}^N \text{ such that } \mathbf{z} \approx \mathbf{A}\mathbf{c} \text{ and } \mathbf{c} \text{ is sparse,} \quad (9)$$

which can be solved by the following minimization problem:

$$\mathbf{c}^\# = \underset{\mathbf{c} \in \mathbb{R}^N}{\operatorname{argmin}} \|\mathbf{A}\mathbf{c} - \mathbf{z}\|_2^2 + \lambda \|\mathbf{c}\|_1 \quad (10)$$

Here, $\lambda > 0$ is the regularization parameter. To forecast T future values of the given trajectory i.e., $\{y(t_{m+i})\}_{i=1}^T$, we use the Euler method:

$$y(t_{m+i}) = y(t_{m+i-1}) + (t_{m+i} - t_{m+i-1})f(\mathbf{h}_{m+i-1}) \quad (11)$$

for all $i = 1, \dots, T$ and $\mathbf{h}_k = [y(t_k), y(t_{k-1}), \dots, y(t_{k-p+1})]^T$ for any integer $k = m, m+1, \dots, m+T$. The summary of our SPADE4 algorithm is given in Algorithm 1 and schematically represented in Figure 1.

Algorithm 1 Algorithm for SPADE4

Input: Input data $\{y(t_k)\}_{k=1}^m$; smoothing parameter s ; function $\phi(\cdot, \boldsymbol{\omega}) = \phi(\langle \cdot, \boldsymbol{\omega} \rangle)$, number of features N , vector of possible regularization parameters $\boldsymbol{\lambda}$, convergence threshold ϵ and total number of iterations `tot_iter`.

Algorithm:

- 1: Build output vector: $\dot{y}(t_1) \leftarrow \frac{y(t_2) - y(t_1)}{(t_2 - t_1)}$; $\dot{y}(t_m) \leftarrow \frac{y(t_m) - y(t_{m-1})}{(t_m - t_{m-1})}$
- 2: **for** $k = 2, 3, \dots, m-1$ **do**
 $\dot{y}(t_k) \leftarrow \frac{y(t_{k+1}) - y(t_{k-1})}{(t_{k+1} - t_{k-1})}$
- 3: **end for**
- 4: **if** $\{y(t_k)\}_{k=1}^m$ is noisy **then**
 $\dot{y}(t_k) \leftarrow \frac{1}{s} \sum_{n=(k+1)-(s-1)}^{k+1} \dot{y}(t_n)$
where $\dot{y}(t_k) = 0 \ \forall \ k \leq 0$ and $k \geq m+1$
- 5: **end if**
- 6: Define $\mathbf{z} = [\dot{y}(t_p), \dot{y}(t_{p+1}), \dots, \dot{y}(t_m)]$
- 7: Draw N random weights $\boldsymbol{\omega}_j \sim \rho(\boldsymbol{\omega})$.
- 8: Define the time-delay data $\mathbf{h}_k = [y(t_k), y(t_{k-1}), \dots, y(t_{k-p+1})]^T$ for $k = p, p+1, \dots, m$.
- 9: Construct random feature matrix $\mathbf{A} = (\phi(\langle \mathbf{h}_i; \boldsymbol{\omega}_j \rangle)) \in \mathbb{R}^{(m-p+1) \times N}$.
- 10: Solve

$$\mathbf{c}^\# = \arg \min_{\mathbf{c} \in \mathbb{R}^N} \|\mathbf{A}\mathbf{c} - \mathbf{z}\|_2^2 + \lambda \|\mathbf{c}\|_1$$

- 11: Learn $\{y(t_k)\}_{k=m+1}^{m+T}$.
 - 12: **for** $i=1, 2, \dots, T$ **do**
 $\hat{f}(\mathbf{h}_{m+i-1}) = \sum_{j=1}^N c_j^\# \phi(\langle \mathbf{h}_{m+i-1}; \boldsymbol{\omega}_j \rangle)$
 $y(t_{m+i}) = y(t_{m+i-1}) + (t_{m+i} - t_{m+i-1})\hat{f}(\mathbf{h}_{m+i-1})$
 - 13: **end for**
-

3 Numerical Experiments on Synthetic Data

In this section, we compare our proposed method and relevant benchmark methods, including the popular SEIR model and the most state-of-the-art $S\mu$ EIR model [54] on synthetic data simulated from the $S\mu$ EIR model. In this simulation study, the input data consists of time series $\{I(t_k)\}_{k=1}^m$ corresponding to the infectious variable $I(t)$ in the $S\mu$ EIR model. Our goal is to obtain a one-week-ahead forecast horizon of this infectious variable. In all experiments, we display the predicted values of the mentioned methods versus the ground truth when varying the size of the training data as the observed trends change (before the peak, after the peak, and around the peak of the epidemic). We also study the robustness of SPADE4 with respect to noise and compare with the benchmark models.

Data generation. We first solve the $S\mu$ EIR model given in Eq. (2) numerically on the time interval $[0, 180]$ (days) with the timestep $\Delta t = 0.01$ and the parameters of the $S\mu$ EIR model:

$$\beta = 3/14, \quad \sigma = 0.25, \quad \mu = 0.75, \quad \gamma = 1/14, \quad P = S(0) + E(0) + I(0) + R(0),$$

and initial conditions are

$$S(0) = 10^6, \quad E(0) = 0, \quad I(0) = 1, \quad R(0) = 0.$$

We normalize the solution by the population P before building the training dataset. The training dataset is either noiseless ($\{I(t_k)\}_{k=1}^m$), or noised ($\{I(t_k) + \varepsilon_k\}_{k=1}^m$), which resembles the reported daily counts of active cases in an outbreak. Note that the inputs are proportions instead of counts in this study. The size of the training data m will be specified in each experiment.

Prediction using SPADE4. For our proposed method, entries of the random weight matrix $\mathbf{W} \in \mathbb{R}^{p \times N}$ are sampled from $\mathcal{N}(0, 1)$ and bias terms $b_j, j \in [N]$ are sampled from $\mathcal{U}(0, 2\pi)$. The activation function is set to $\phi(\cdot) = \text{ReLU}(\cdot)$, the number of random weights is $N = 50m$, where m is the number of training points, and the time delay $\tau = 1$. We choose the embedding dimension $p = 2d + 1$, where $d = 4$ is the dimension of the original system. The ℓ_1 -regularization parameter λ is selected by the model from a range of possible values, $\lambda \in [10^{-6}, 5 \times 10^{-6}, 10^{-7}, 5 \times 10^{-7}, 10^{-8}, 5 \times 10^{-8}, 10^{-9}, 5 \times 10^{-9}]$. Using the training data, we obtain the learned coefficients \mathbf{c} by solving the optimization problem (10) and forecast the proportion of daily active cases $\hat{I}_{ours}(t)$ using Equation (11).

Prediction using benchmark models. For benchmark models, we fit the data with $S\mu$ EIR and SEIR models to learn the models' parameters (from 100 possible random initializations), which are $(\beta, \sigma, \mu, \gamma)$ for the $S\mu$ EIR model and (β, σ, γ) for SEIR given in Equation (1).

Prediction accuracy. For all the methods, accuracy of predicting the trajectory of a novel pathogen outbreak (such as COVID-19) is measured using relative test error which is calculated as

$$\text{Error}(I, \hat{I}_{model}) = \sqrt{\frac{\sum_{k=m+1}^{m+7} |I(t_k) - \hat{I}_{model}(t_k)|^2}{\sum_{k=m+1}^{m+7} |I(t_k)|^2}}, \quad (12)$$

where I denotes the true values and \hat{I}_{model} are the predicted values of a model.

3.1 Results on Noiseless Simulated Data

We first present numerical results on simulated data without noise where we evaluate model performance during key moments of the epidemic, i.e., before, around, and after the peak of the curve. For before and after the peak, we consider data points upto 81^{st} and 125^{th} days (given by the dashed vertical lines in the top left plot of Figure 2) out of 180 days, respectively as the training set, and predict for the next seven days. The corresponding predicted curves of the one-week-ahead-forecast horizon are shown in the middle first row and the top right plot of Figure 2. For assessing model performance around the changing slope of the trajectory, we consider the number of training points $m \in \{97, 100, 104, 108, 111\}$ and plot the predicted curves of our proposed method and the two benchmark models for the one-week-ahead forecast in the second row of Figure 2. We observe from Figure 2 that the best performance is given by the benchmark model fitted with $S\mu EIR$ (green curves), closely by our proposed method (blue curves) and the SEIR model (magenta curves). This is an expected outcome considering that we are fitting the benchmark model with the same model from which data was simulated. However, in real world applications, there are irregularities data which can make the noiseless case too idealistic. So in the following section, we add noise to the input data and then compare the performance of benchmark models to our SPADE4.

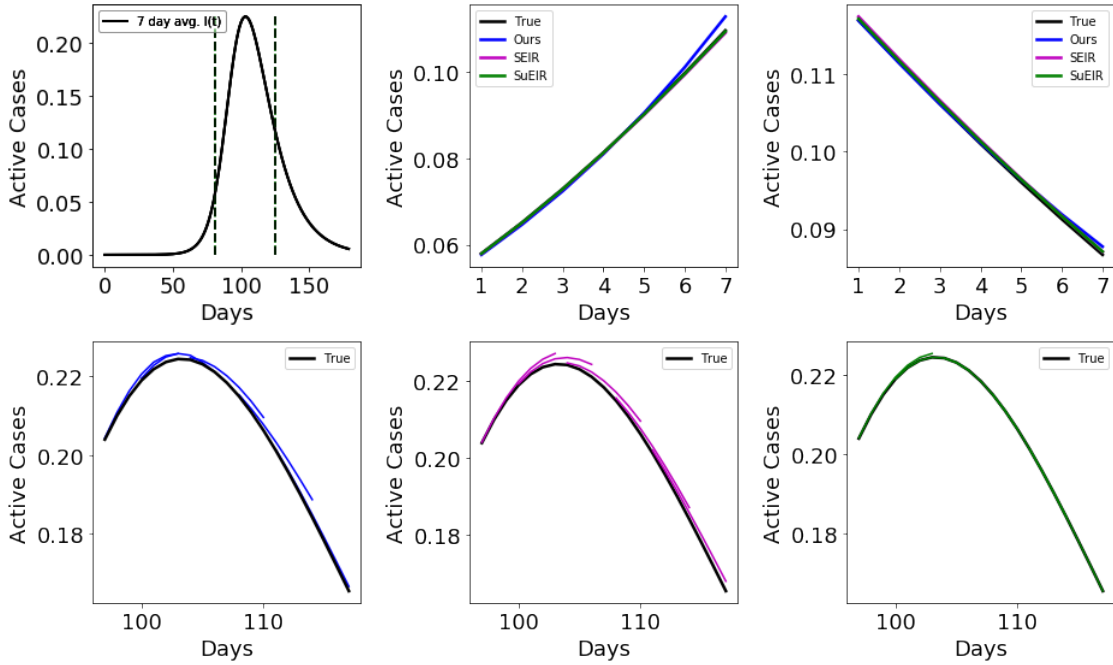


Figure 2: Results on noiseless simulated data. First row: Noiseless training datasets from 0 upto 81^{st} and 125^{th} days out of 180 days (top left). The next two figures are the predicted values of the infectious variable $I(t)$ in the next seven days using SPADE4 (blue), SEIR model (magenta), and $S\mu EIR$ model (green) correspond to those two training datasets versus ground truth (black). Second row: Prediction of $I(t)$ for next seven days around the peak of the wave using SPADE4 (blue), SEIR model (magenta), and $S\mu EIR$ model (green) versus ground truth (black).

3.2 Results on Noisy Simulated Data

In this section we consider noisy input data. As before, the data is simulated from Equation (2) with the parameters described above. The input data with noise is given by,

$$I_{\text{noisy}}(t) = I(t) + \varepsilon \max(|I(t)|), \quad (13)$$

where $I(t)$ is the clean data, $\varepsilon \sim \mathcal{N}(0, \eta)$, and η is the noise level. For all experiments involving noisy input data, we pre-process the input data by considering seven-day average of $I(t)$. This is done to take care of data irregularities and resemble set up in practice. For our SPADE4, an additional convolution based smoothing filter with parameter $s = 15$ is also used on the output vector $\{\dot{I}(t_k)\}_{k=1}^m$. This is done to minimize noise amplification from the use of finite difference approximations to obtain $\{\dot{I}(t_k)\}_{k=1}^m$. Similar to the setup in Section 3.1, we consider the number of training points $m \in \{81, 97, 100, 104, 108, 111, 125\}$ days and plot the one-week-ahead forecast. We consider 5% noise level, i.e., $\eta = 0.05$ and plot the results in Figure 3. Experimental results with $\eta = 0.02$ are given in the appendix.

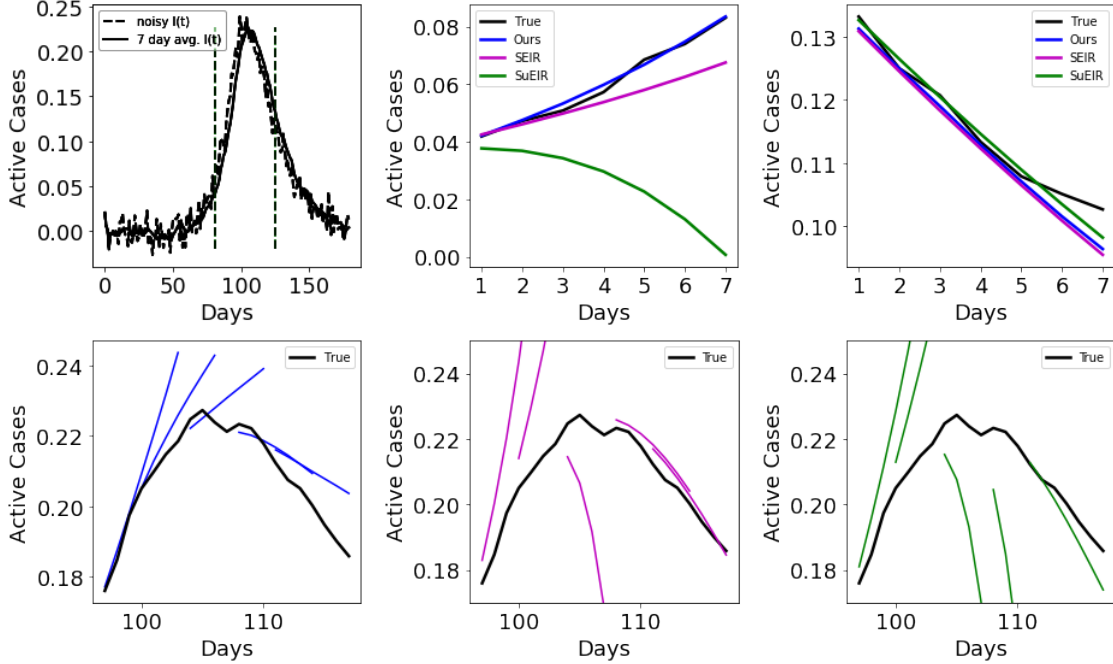


Figure 3: Results on simulated data with 5% noise added to input data. First row: Noiseless training datasets from 0 upto 81st and 125th days out of 180 days (top left). The next two figures are the predicted values of the infectious variable $I(t)$ in the next seven days using SPADE4 (blue), SEIR model (magenta), and $S\mu$ EIR model (green) correspond to those two training datasets versus ground truth (black). Second row: Prediction of $I(t)$ for next seven days around the peak of the wave using SPADE4 (blue), SEIR model (magenta), and $S\mu$ EIR model (green) versus ground truth (black).

Before the peak, the one-week-ahead forecast of our SPADE4 outperforms the SEIR and the $S\mu$ EIR model in both cases of the noise level. After the peak, the prediction results of SPADE4 and the SEIR model are comparable and are better than those obtained from the $S\mu$ EIR (see top

row of Figure 3). Around the peak, (see bottom row of Figure 3), we observe that SPADE4 quickly picks up the changing slope in the wave. On the other hand, the benchmark models give unreliable results at some points in the curve. Both benchmark models overpredict the number of active cases for $m \in \{97, 100\}$ and underpredict the number of active cases for $m = 104$.

The superior performance of SPADE4 can be seen more clearly from Figure 4 where we plot the validation errors for our model and the benchmark models fitted different sizes of training data m and noise levels $\eta = 0.02$ and $\eta = 0.05$. We see that SPADE4 has low relative error consistently while the errors for the other models tend to fluctuate to a higher error at certain points. The performance of the benchmark models are highly influenced by the number of training points, noise level as well as the nature of the curve while our proposed SPADE4 is robust to all these factors affecting input data.

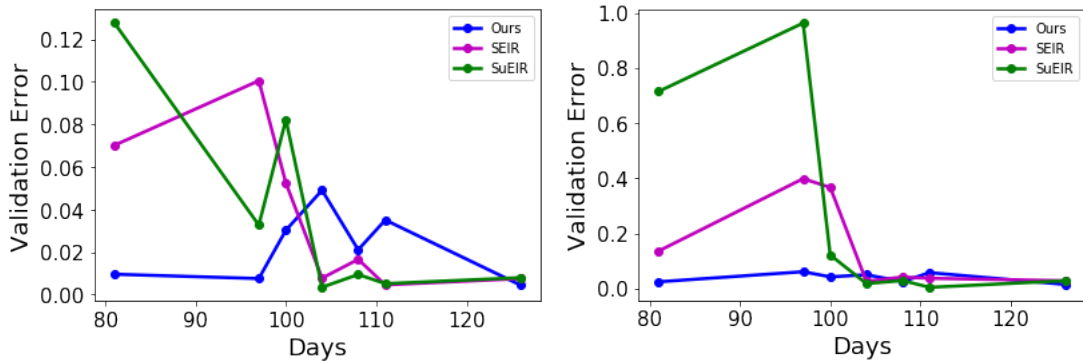


Figure 4: Validation errors based on various size of the training data $m \in \{81, 97, 101, 104, 108, 112, 126\}$ for the noise level $\eta = 0.02$ (left) and $\eta = 0.05$ (right).

4 Numerical Experiments on Real Datasets

In this section, we demonstrate the performance of SPADE4 on various real datasets, including daily active cases of 2019 Coronavirus (COVID-19) in Canada¹ as well as cumulative cases of Ebola in Guinea², Zika virus in Giradot [38], and influenza A/H7N9 in China³. The training data for the benchmark models is given by $I(t)$ for the COVID-19 dataset and by the variable $I(t) + R(t)$ for the remaining datasets. For each dataset, we compare the one-week-ahead forecasts of SPADE4 with benchmark methods including SEIR and S_μ EIR models across important moments in the epidemic.

4.1 Data from Daily Active Cases of COVID-19 in Canada

In this section, we study the one-week-ahead forecast of the number of active COVID-19 cases in Canada (see Figure 5) upto the fifth wave of COVID19. Each wave is approximately given by the black vertical lines in Figure 5. We notice that the first four waves are similar in terms of the wavelength as well as the amplitude. On the other hand, the fifth wave however is different since it is driven by a much more infectious Omicron variant and hence has a short wavelength with a

¹<https://health-infobase.canada.ca/covid-19/epidemiological-summary-covid-19-cases.html>

²<https://www.kaggle.com/datasets/imdevskp/ebola-outbreak-20142016-complete-dataset>

³<https://datadryad.org/stash/dataset/doi:10.5061/dryad.2g43n>

higher amplitude. Therefore, we examine the forecast within the second (from day 200 to day 380) and the fifth waves (from day 650 to day 704) of the COVID19 in Canada.

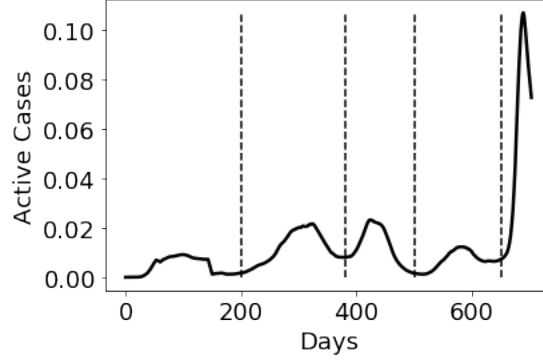


Figure 5: Proportion of daily active COVID-19 cases in Canada from the beginning of the pandemic to the end of fifth wave.

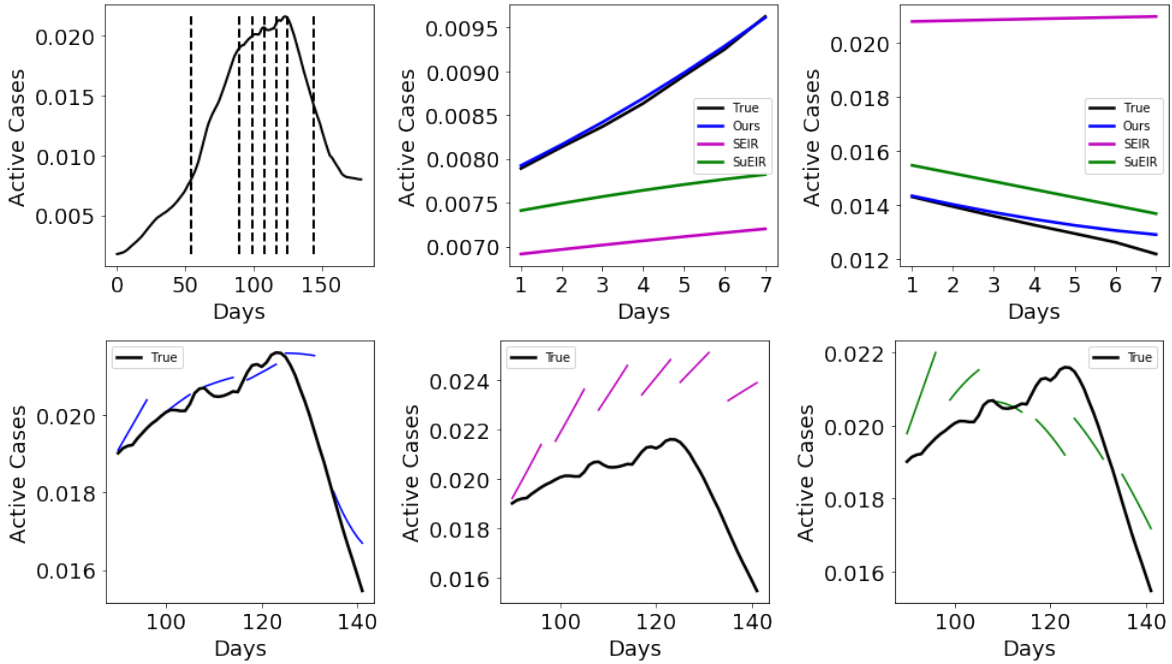


Figure 6: Results on second wave of COVID-19 in Canada. First row: Second wave from 0 upto 54^{th} and 144^{th} days out of 180 days (top left). The next two figures are the predicted values of the infectious variable $I(t)$ in the next seven days using SPADE4 (blue), SEIR model (magenta), and $S\mu$ EIR model (green) correspond to those two training datasets versus ground truth (black). Second row: Prediction of $I(t)$ for next seven days around the peak of the wave using SPADE4 (blue), SEIR model (magenta), and $S\mu$ EIR model (green) versus ground truth (black).

The anomalies in how data were reported, such as the under-reporting of cases on weekends and the backlog cases reported later, can lead to noisy dataset. Hence, we consider seven day average of

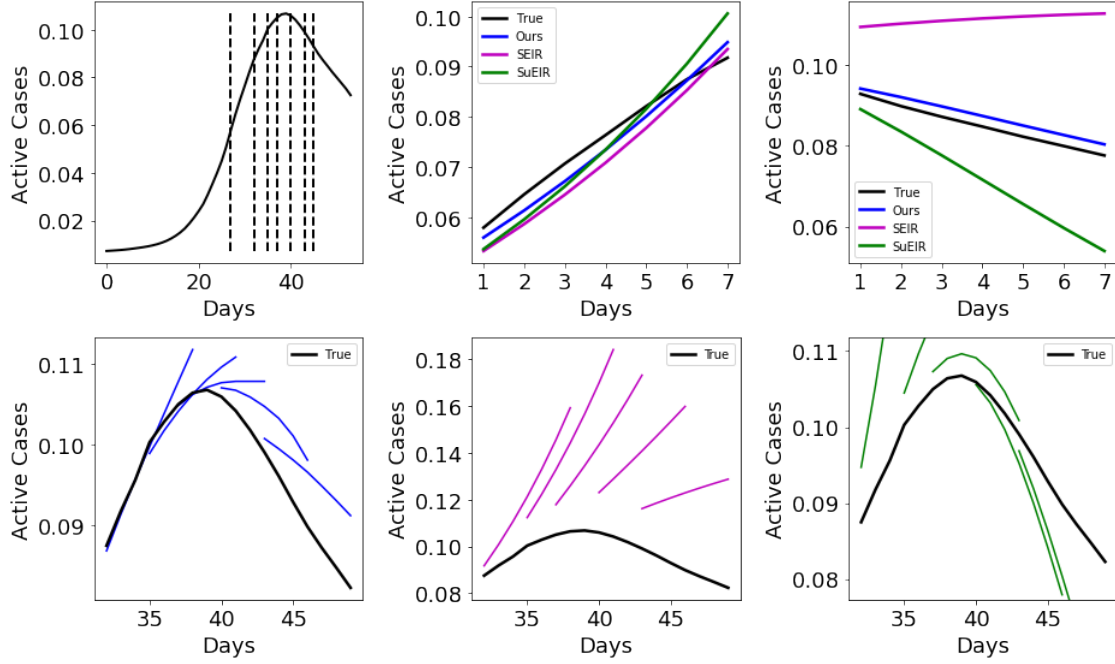


Figure 7: Results on fifth wave of COVID-19 in Canada. First row: Second wave from 0 upto 27th and 46th days out of 180 days (top left). The next two figures are the predicted values of the infectious variable $I(t)$ in the next seven days using SPADE4 (blue), SEIR model (magenta), and $S\mu$ EIR model (green) correspond to those two training datasets versus ground truth (black). Second row: Prediction of $I(t)$ for next seven days around the peak of the wave using SPADE4 (blue), SEIR model (magenta), and $S\mu$ EIR model (green) versus ground truth (black).

the given data as the ground truth. For the initial conditions required by the benchmark models, we choose the initial values of the variables $I(t_0) = I_0$, $R(t_0) = 0$, where I_0 is the first data point in the training set. Since the initial exposed population is not known, we let the model choose the best estimate of $E(t_0)$ from $\{kI_0 : k \in \{0, 1, 5, 10, 15, 20, 25, 50, 80\}\}$, which is the value of $E(t_0)$ that gives the smallest l_2 -squared error over the training set. Finally, the initial susceptible variable is given by $S(t_0) = P - E(t_0) - I(t_0)$, where P is the approximate population of Canada, $P = 3.8 \times 10^7$. To avoid negligible values when the population P is extremely large compared to the number of active cases, we normalize the training data by dividing the entire dataset by $c * P$, where $c \in (0, 1]$. Here, we choose $c = 0.1$. Finally, for both the second and the fifth waves, we consider the number of training data m as the observed trends change, including the trends before the peak, around the peak, and after the peak. More precisely, m is chosen from the set $\{54, 90, 99, 108, 117, 126, 135, 144\}$ for the second wave and from the set $m \in \{27, 32, 35, 38, 41, 43, 46\}$ for the fifth wave (see the top left figures in Figure 6 and Figure 7). Note that m corresponds to the number of days starting from the starting date of a wave.

The forecast result illustrates the advantage of our method compared to the benchmark models. More precisely, the forecasts suggested by SPADE4 (blue curves in Figures 6 and 7) are closest to the true curve (in black) and it successfully picks up the changing nature of the curve around the peak quickly and adapts to the downward trend of the true curve. With the SEIR model, as the training data varies across before, around to after the peak (second row and top right plots in

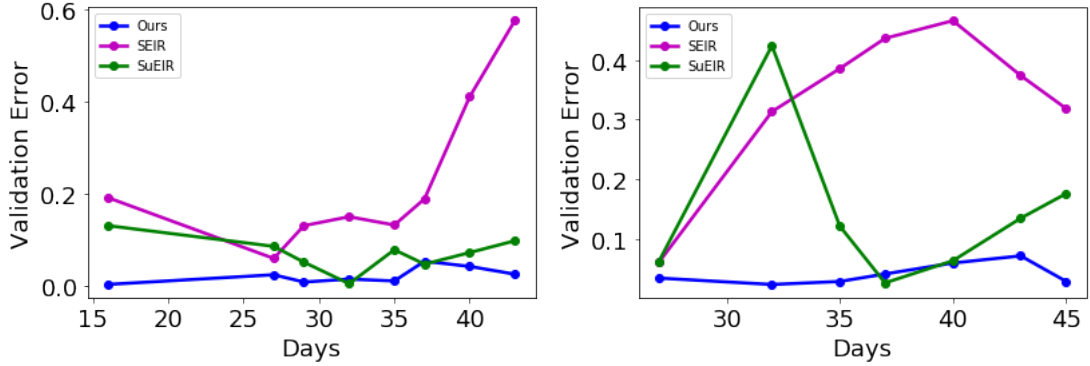


Figure 8: Validation error plot with various number of training points for our model and the benchmark models on second (left) and fifth (right) wave of COVID-19 dataset.

Figures 6 and 7), it tends to move from underprediction to overprediction to an extent where it is completely away from the true curve after the peak. The $S\mu EIR$ model starts with underprediction and moves on to a mix of overprediction and underprediction inconsistently without picking up the changing slope of the trajectory as the size of training data varies (second row and top right plots in Figures 6 and 7). Figure 8 plots the relative validation errors versus various training sizes of our SPADE4 and benchmark models during both waves. SPADE4 outperforms benchmark models with the smallest relative validation errors. We also observe that the $S\mu EIR$ model performs better than the SEIR model for most chosen points. One of the potential reasons is because the $S\mu EIR$ model takes into account unreported cases.

4.2 Data from Cumulative Cases of Ebola in Guinea, Zika in Giradot and influenza A/H7N9 in China

In this section, we use data based on cumulative cases of Ebola in Guinea, Zika in Giradot and influenza A/H7N9 in China. For each dataset, the parameters based on size of dataset, population P used for normalization of the dataset, preprocessing constant, size of training set and forecast horizon have been summarized in Table 1. The initial conditions are chosen as $S(t_0) = P - E(t_0) - I(t_0)$, $I(t_0) = I_0$, $R(t_0) = 0$, where I_0 is the first data point in each dataset and we estimate $E(t_0)$ from $\{kI_0 : k \in \{0, 1, 5, 10, 15, 20, 25, 50, 80\}\}$, which is the value of $E(t_0)$ that gives the smallest l_2 -squared error over the training set. As in Section 4.1, we let the model choose the best estimate of $E(t_0)$. A convolution filter with the parameter $s = 10$ (see Equation (7)) is used on the derivative vector. We test SPADE4 on different sizes of training sets with cardinality m (see Table 1 for values of m considered). Comparison with the benchmark method is done using one-week-forecast horizon of the proportion of cumulative cases.

The one-week-ahead forecasts of the Ebola, Zika and flu datasets are given in Figure 9. From the second column in Figure 9, we can see that the benchmark methods with SEIR and $S\mu EIR$ have a tendency to underpredict for Zika and flu datasets when the epidemic curve has a sharp slope and number of training points is less. For the Ebola dataset, $S\mu EIR$ model learns well with less training data, however the SEIR model overpredicts far away from the true curve. At this point however, forecasts suggested by SPADE4 is closest to the true values. Towards the end of the curve given in the third column of Figure 9, an increase in training data improves the $S\mu EIR$ benchmark

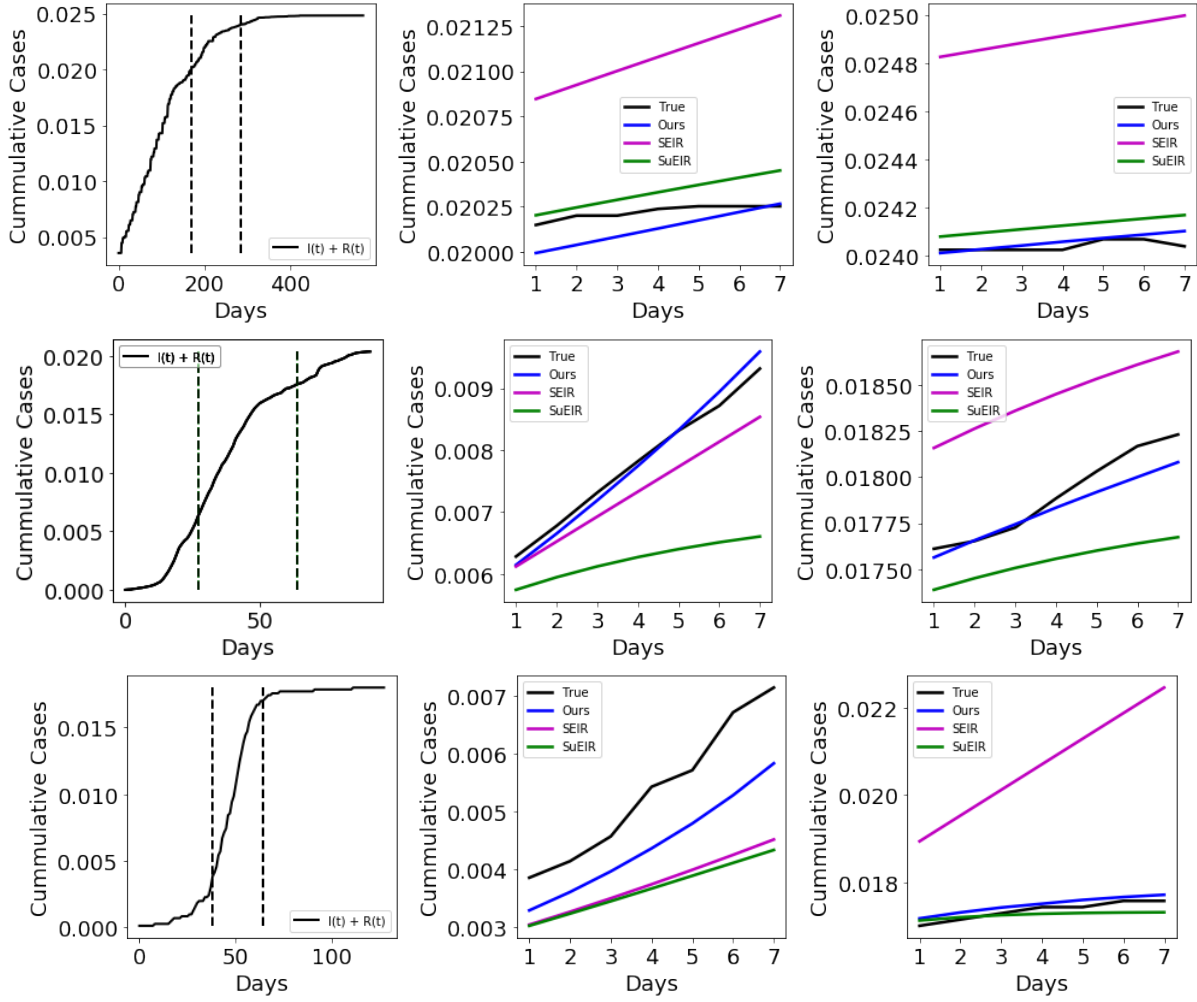


Figure 9: First column presents Ebola (top), Zika (center) and influenza A/H7N9 (bottom) datasets where the training data is from day 0th to the dashed vertical lines. The next two columns present the corresponding one-week ahead forecasts of our SPADE4 (in blue), SEIR (in magenta), and $S\mu$ EIR (in green) versus ground truth (in black).

Data	Total Data	Population	c	m (days)	Prediction Interval
Ebola Data from Guinea	572	135×10^6	10^{-2}	172	173-179
				286	287-293
Zika Data from Giradot	93	95×10^3	1	27	28-34
				65	66-72
Influenza A/H7N9 Data from China	128	7×10^8	10^{-5}	44	45-51
				64	65-71

Table 1: Parameters corresponding to datasets for Ebola, Zika and influenza A/H7N9.

method (green curves) predictions which are much closer to the true values especially for Ebola and flu datasets. The SEIR method predictions are still far away irrespective of the increase in training points as the method struggles to learn the changing nature of the trajectory. Predictions of SPADE4 remain consistently close to the true values with slight improvement with increase in the size of training data. This can be seen more clearly in Table 2 where relative errors on the one-week-ahead horizon has been summarized. The results demonstrates that the performance of the benchmark method is dependent on the knowledge of target model, nature of the epidemic and the number of data points. Fitting to an incorrect target model or scarce training data can affect prediction accuracy. However, SPADE4 can predict close to the true values without any prior knowledge of the underlying model.

Data	m	SPADE4	SEIR	S μ EIR
Ebola Data from Guinea	172	0.0053	0.0428	0.0058
	286	0.0012	0.0365	0.0036
Zika Data from Giradot	27	0.0204	0.0638	0.2185
	65	0.0055	0.0302	0.0213
Influenza A/H7N9 Data from China	38	0.1783	0.3178	0.3359
	64	0.0079	0.2017	0.0097

Table 2: Relative error over one-week-ahead forecast horizon for different sizes of training data for the datasets corresponding to Ebola, Zika and influenza A/H7N9.

4.3 Prediction Interval

We propose a simple method to construct the prediction interval for SPADE4. The main idea is using part of the training data to estimate the variance $\hat{\sigma}(t)$ of $\hat{I}_{ours}(t)$. Then, the 95% prediction interval is $\hat{I}_{ours}(t) \pm 1.96\hat{\sigma}(t)$. The detail of our construction method is outlined in Algorithm 2. To illustrate the performance of this method, we construct the prediction interval for the Ebola, Zika and influenza A/H7N9 datasets using the same setting as in Section 4.2. We can see that the true curve lies inside the shaded region of the 95% prediction interval (Figure 10).

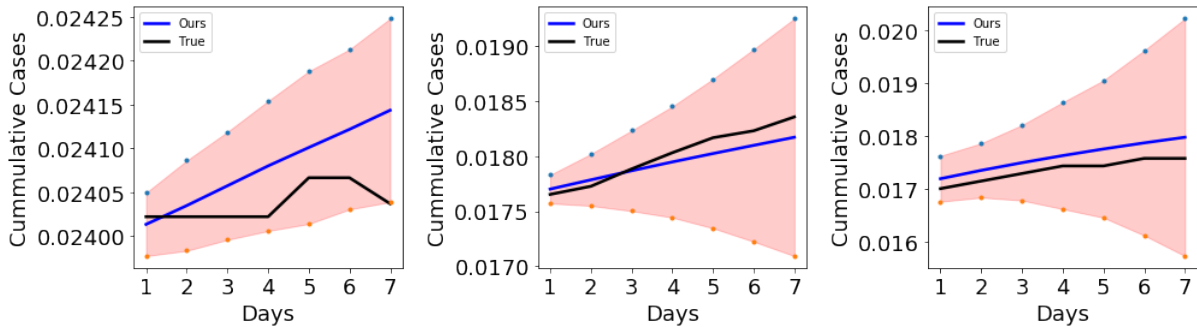


Figure 10: Prediction Interval for the Ebola dataset with $m = 286$ ($m_1 = 266$ and $m_2 = 286$), Zika dataset with $m = 65$ ($m_1 = 45$ and $m_2 = 65$) and influenza A/H7N9 dataset with $m = 64$ ($m_1 = 44$ and $m_2 = 64$).

Algorithm 2 Prediction Interval of SPADE4

Given: Data $\{I(t_k)\}_{k=1}^{m_2}$; Forecast window T ; a number $m_1 < m_2 - T$

To find: 95% prediction interval for $\{I(t_k)\}_{k=m_2+1}^{m_2+T}$.

Algorithm:

- 1: Initialize $V = [\mathbf{v}_1, \mathbf{v}_2, \dots, \mathbf{v}_{m_2-m_1-T}] \in \mathbb{R}^{T \times (m_2-m_1-T)}$ and $\hat{\Sigma} = [\hat{\sigma}_1, \hat{\sigma}_2, \dots, \hat{\sigma}_T] \in \mathbb{R}^T$.
 - 2: **for** $i = 1, 3, \dots, m_2 - m_1 - T$ **do**
 $\{\hat{I}_{ours}(t_k)\}_{k=m_1+i}^{m_1+i+T} \leftarrow \text{SPADE4}(\{I(t_k)\}_{k=1}^{m_1+i-1})$
 $\mathbf{v}_i \leftarrow [\hat{I}_{ours}(t_{m_1+i}) - I(t_{m_1+i}), \hat{I}_{ours}(t_{m_1+i+1}) - I(t_{m_1+i+1}), \dots, \hat{I}_{ours}(t_{m_1+i+T}) - I(t_{m_1+i+T})]^T$
 - 3: **end for**
 - 4: **for** $j = 1, 2, \dots, T$ **do**

$$\hat{\sigma}_j = \sqrt{\frac{1}{m_2 - m_1 - T} \sum_{k=1}^{m_2-m_1-T} V[k, j]^2}$$
 - 5: **end for**
 - 6: Find $\{\hat{I}_{ours}(t_k)\}_{k=m_2+1}^{m_2+T} \leftarrow \text{SPADE4}(\{I(t_k)\}_{k=1}^{m_2})$
 - 7: Prediction intervals: $[\hat{I}(t_{m_2+1}) \pm \hat{\sigma}_1 * 1.96, \hat{I}(t_{m_2+2}) \pm \hat{\sigma}_2 * 1.96, \dots, \hat{I}(t_{m_2+T}) \pm \hat{\sigma}_T * 1.96]$
-

4.4 Stability

Since our proposed method SPADE4 uses random features as a basis, in all our experiments above, we make use of a fixed seed to ensure the results are consistent over multiple execution of the simulations. However, in this section we provide numerical evidence of the stability of SPADE4 with respect to the random basis generated for each simulation. Figure 11 gives all the possible predicted curves for the second wave of COVID-19 in Canada with different sizes of training data using SPADE4 (shaded in blue) over one hundred randomly generated basis along with the predictions of the benchmark methods. We can see that all the predictions made by SPADE4 are closest to the true curve (in black) in comparison to the other methods depicting that SPADE4 performs well consistently irrespective of the random basis generated.

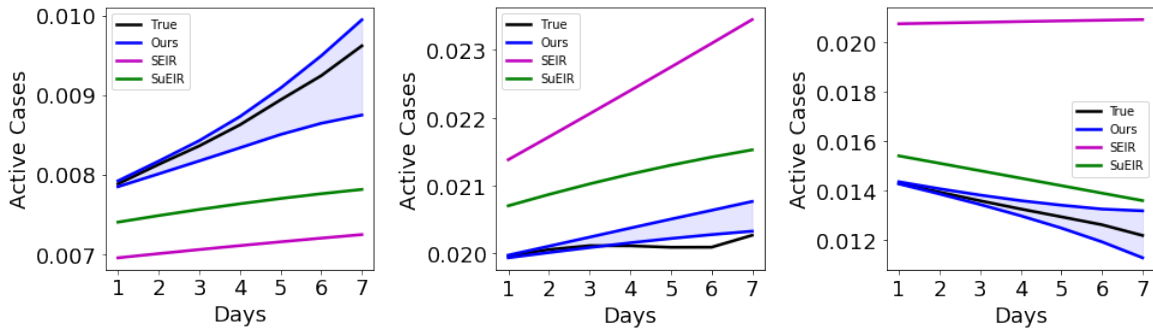


Figure 11: Predicted seven-day forecast curves using 100 runs of SPADE4 (shaded in blue) and the benchmark methods (SEIR model in magenta and $S_\mu\text{EIR}$ model in green) before the peak, at the peak and after the peak.

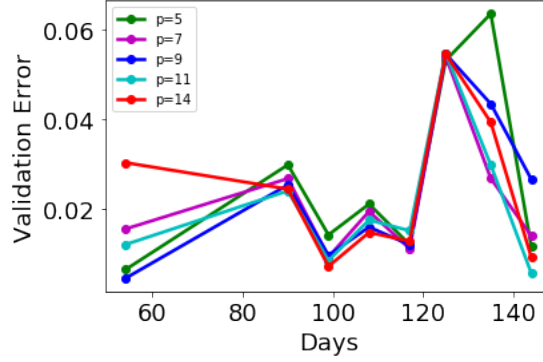


Figure 12: Validation error plot with various number of training points for SPADE4 with $p \in \{5, 7, 9, 11, 14\}$ for the second wave of COVID-19 in Canada.

4.5 Varying Embedding Dimension

In this section, we demonstrate the stability of our method with respect to the choice of the embedding dimension p . We plot the validation error for one-week ahead forecasts for the second wave of COVID-19 in Canada with varying p and plot them in Figure 12. We use $p = 9$ in all our experiments since we follow the population division suggested by one of the most popular SEIR model in epidemiology. Since $d = 4$ in SEIR and $S\mu$ EIR models, we choose $p = 2d + 1 = 9$. The results in Figure 12 demonstrate the fact that using $p = 9$ gives consistently good results across different sizes of training data. While values of $p < 9$ do not perform the best, the error does improve for some cases when $p > 9$. However for small input data, a large value of p is not feasible since it would further reduce the training data after the use of time delay embedding map. Thus, while the embedding dimension p is a hyperparameter worthy of further exploration, our experiments suggest that choosing $p = 2d + 1$ outperforms other choices when both, the size of input data and the validation error is taken into account.

5 Discussion and Conclusion

Short-term forecasts of an epidemic based trajectory serve as a communication channel between the scientific community and decision makers. It helps in taking informed short-term decisions such as allocation of medical supplies, healthcare staffing needs, lockdowns and closures. We propose a delay embedding based model SPADE4 which forecasts the trajectory (daily active cases or cumulative cases) in a one-week-forecast horizon. We compare SPADE4 with benchmark methods with SEIR and $S\mu$ EIR fitting. Our experiments on simulated and real datasets show that SPADE4 can provide a reliable and comparatively accurate forecast that exceeds the performance the benchmark method. While some knowledge of target model and initial values are required by the benchmark model, SPADE4 has no such prerequisites for its performance. Using existing theoretical results on delay embedding and sparse random feature models, we show that the choice of hyperparameters made by us for SPADE4 are reasonable for its performance. Additionally we also provide results to show that the predictions given by SPADE4 is stable with respect to the basis chosen as well as our choice of the embedding dimension p . Further direction of this work involves considering data from diseases which are oscillating in nature and some theoretical understanding on the ways to choose

the embedding dimension.

Acknowledgement

LSTH was supported by the Canada Research Chairs program, the NSERC Discovery Grant RGPIN-2018-05447, and the NSERC Discovery Launch Supplement DGECR-2018-00181. E. Saha and G. Tran were supported by the NSERC Discovery Grant and the NSERC Discovery Launch Supplement.

References

- [1] C. L. Althaus. Estimating the reproduction number of Ebola virus (EBOV) during the 2014 outbreak in West Africa. *PLoS currents*, 6, 2014.
- [2] I. Ayed, E. de Bézenac, A. Pajot, J. Brajard, and P. Gallinari. Learning dynamical systems from partial observations. *arXiv preprint arXiv:1902.11136*, 2019.
- [3] K. Bhattacharya, B. Hosseini, N. B. Kovachki, and A. M. Stuart. Model reduction and neural networks for parametric pdes. *arXiv preprint arXiv:2005.03180*, 2020.
- [4] M. G. Blum and V. C. Tran. HIV with contact tracing: a case study in approximate Bayesian computation. *Biostatistics*, 11(4):644–660, 2010.
- [5] D. S. Broomhead and G. P. King. Extracting qualitative dynamics from experimental data. *Physica D: Nonlinear Phenomena*, 20(2-3):217–236, 1986.
- [6] S. L. Brunton, B. W. Brunton, J. L. Proctor, E. Kaiser, and J. N. Kutz. Chaos as an intermittently forced linear system. *Nature Communications*, 8(1):1–9, 2017.
- [7] S. L. Brunton, J. L. Proctor, and J. N. Kutz. Discovering governing equations from data by sparse identification of nonlinear dynamical systems. *Proceedings of the National Academy of Sciences*, 113(15):3932–3937, 2016.
- [8] S. Cauchemez and N. M. Ferguson. Likelihood-based estimation of continuous-time epidemic models from time-series data: application to measles transmission in london. *Journal of the Royal Society Interface*, 5(25):885–897, 2008.
- [9] K. P. Champion, S. L. Brunton, and J. N. Kutz. Discovery of nonlinear multiscale systems: Sampling strategies and embeddings. *SIAM Journal on Applied Dynamical Systems*, 18(1):312–333, 2019.
- [10] E. Y. Cramer, E. L. Ray, V. K. Lopez, J. Bracher, A. Brennen, A. J. Castro Rivadeneira, A. Gerding, T. Gneiting, K. H. House, Y. Huang, et al. Evaluation of individual and ensemble probabilistic forecasts of COVID-19 mortality in the United States. *Proceedings of the National Academy of Sciences*, 119(15):e2113561119, 2022.
- [11] V. Dukic, H. F. Lopes, and N. G. Polson. Tracking epidemics with Google flu trends data and a state-space SEIR model. *Journal of the American Statistical Association*, 107(500):1410–1426, 2012.

- [12] R. González-García, R. Rico-Martínez, and I. G. Kevrekidis. Identification of distributed parameter systems: A neural net based approach. *Computers & Chemical Engineering*, 22:S965–S968, 1998.
- [13] P. Goyal and P. Benner. Discovery of nonlinear dynamical systems using a runge–kutta inspired dictionary-based sparse regression approach. *Proceedings of the Royal Society A*, 478(2262):20210883, 2022.
- [14] A. Hashemi, H. Schaeffer, R. Shi, U. Topcu, G. Tran, and R. Ward. Generalization bounds for sparse random feature expansions. *Applied and Computational Harmonic Analysis*, 62:310–330, 2023.
- [15] L. S. T. Ho, F. W. Crawford, and M. A. Suchard. Direct likelihood-based inference for discretely observed stochastic compartmental models of infectious disease. *The Annals of Applied Statistics*, 12(3):1993–2021, 2018.
- [16] L. S. T. Ho, J. Xu, F. W. Crawford, V. N. Minin, and M. A. Suchard. Birth/birth-death processes and their computable transition probabilities with biological applications. *Journal of Mathematical Biology*, 76(4):911–944, 2018.
- [17] J. Huke. Embedding nonlinear dynamical systems: A guide to takens’ theorem. 2006.
- [18] A. Jacot, B. Simsek, F. Spadaro, C. Hongler, and F. Gabriel. Implicit regularization of random feature models. In *International Conference on Machine Learning*, pages 4631–4640. PMLR, 2020.
- [19] J.-N. Juang and R. S. Pappa. An eigensystem realization algorithm for modal parameter identification and model reduction. *Journal of Guidance, Control, and Dynamics*, 8(5):620–627, 1985.
- [20] E. Kaiser, J. N. Kutz, and S. L. Brunton. Sparse identification of nonlinear dynamics for model predictive control in the low-data limit. *Proceedings of the Royal Society A*, 474(2219):20180335, 2018.
- [21] M. Kamb, E. Kaiser, S. L. Brunton, and J. N. Kutz. Time-delay observables for koopman: Theory and applications. *SIAM Journal on Applied Dynamical Systems*, 19(2):886–917, 2020.
- [22] I. E. Lagaris, A. Likas, and D. I. Fotiadis. Artificial neural networks for solving ordinary and partial differential equations. *IEEE Transactions on Neural Networks*, 9(5):987–1000, 1998.
- [23] S. Le Clainche and J. M. Vega. Higher order dynamic mode decomposition. *SIAM Journal on Applied Dynamical Systems*, 16(2):882–925, 2017.
- [24] Z. Li, N. Kovachki, K. Azizzadenesheli, B. Liu, K. Bhattacharya, A. Stuart, and A. Anandkumar. Fourier neural operator for parametric partial differential equations. *arXiv preprint arXiv:2010.08895*, 2020.
- [25] A. T. Lin, D. Eckhardt, R. Martin, S. Osher, and A. S. Wong. Parameter inference of time series by delay embeddings and learning differentiable operators. *arXiv preprint arXiv:2203.06269*, 2022.

- [26] L. Lu, P. Jin, and G. E. Karniadakis. Deeponet: Learning nonlinear operators for identifying differential equations based on the universal approximation theorem of operators. *arXiv preprint arXiv:1910.03193*, 2019.
- [27] L. Lu, X. Meng, Z. Mao, and G. E. Karniadakis. Deepxde: A deep learning library for solving differential equations. *SIAM Review*, 63(1):208–228, 2021.
- [28] B. Lusch, J. N. Kutz, and S. L. Brunton. Deep learning for universal linear embeddings of nonlinear dynamics. *Nature Communications*, 9(1):1–10, 2018.
- [29] N. M. Mangan, J. N. Kutz, S. L. Brunton, and J. L. Proctor. Model selection for dynamical systems via sparse regression and information criteria. *Proceedings of the Royal Society A: Mathematical, Physical and Engineering Sciences*, 473(2204):20170009, 2017.
- [30] K. S. Narendra and K. Parthasarathy. Neural networks and dynamical systems. *International Journal of Approximate Reasoning*, 6(2):109–131, 1992.
- [31] N. H. Nelsen and A. M. Stuart. The random feature model for input-output maps between banach spaces. *SIAM Journal on Scientific Computing*, 43(5):A3212–A3243, 2021.
- [32] T. Qin, K. Wu, and D. Xiu. Data driven governing equations approximation using deep neural networks. *Journal of Computational Physics*, 395:620–635, 2019.
- [33] A. Rahimi and B. Recht. Random features for large-scale kernel machines. In *NIPS*, volume 3, page 5. Citeseer, 2007.
- [34] A. Rahimi and B. Recht. Uniform approximation of functions with random bases. In *2008 46th Annual Allerton Conference on Communication, Control, and Computing*, pages 555–561. IEEE, 2008.
- [35] A. Rahimi and B. Recht. Weighted sums of random kitchen sinks: replacing minimization with randomization in learning. In *NIPS*, pages 1313–1320. Citeseer, 2008.
- [36] M. Raissi, P. Perdikaris, and G. E. Karniadakis. Physics-informed neural networks: A deep learning framework for solving forward and inverse problems involving nonlinear partial differential equations. *Journal of Computational Physics*, 378:686–707, 2019.
- [37] N. Richardson, H. Schaeffer, and G. Tran. Srmd: Sparse random mode decomposition, 2022.
- [38] D. P. Rojas, N. E. Dean, Y. Yang, E. Kenah, J. Quintero, S. Tomasi, E. L. Ramirez, Y. Kelly, C. Castro, G. Carrasquilla, et al. The epidemiology and transmissibility of Zika virus in Girardot and San Andres island, Colombia, September 2015 to January 2016. *Eurosurveillance*, 21(28):30283, 2016.
- [39] A. Rudi and L. Rosasco. Generalization properties of learning with random features. In *NIPS*, pages 3215–3225, 2017.
- [40] S. H. Rudy, S. L. Brunton, J. L. Proctor, and J. N. Kutz. Data-driven discovery of partial differential equations. *Science Advances*, 3(4):e1602614, 2017.

- [41] E. Saha, H. Schaeffer, and G. Tran. Harfe: Hard-ridge random feature expansion. *arXiv preprint arXiv:2202.02877*, 2022.
- [42] H. Schaeffer. Learning partial differential equations via data discovery and sparse optimization. *Proceedings of the Royal Society A: Mathematical, Physical and Engineering Sciences*, 473(2197):20160446, 2017.
- [43] H. Schaeffer, G. Tran, and R. Ward. Extracting sparse high-dimensional dynamics from limited data. *SIAM Journal on Applied Mathematics*, 78(6):3279–3295, 2018.
- [44] V. Sitzmann, J. Martel, A. Bergman, D. Lindell, and G. Wetzstein. Implicit neural representations with periodic activation functions. *Advances in Neural Information Processing Systems*, 33:7462–7473, 2020.
- [45] W.-H. Su, C.-S. Chou, and D. Xiu. Deep learning of biological models from data: applications to ode models. *Bulletin of Mathematical Biology*, 83(3):1–19, 2021.
- [46] F. Takens. Detecting strange attractors in turbulence. In *Dynamical Systems and Turbulence, Warwick 1980*, pages 366–381. Springer, 1981.
- [47] G. Tran and R. Ward. Exact recovery of chaotic systems from highly corrupted data. *Multiscale Modeling & Simulation*, 15(3):1108–1129, 2017.
- [48] G. Uribarri and G. B. Mindlin. Dynamical time series embeddings in recurrent neural networks. *Chaos, Solitons & Fractals*, 154:111612, 2022.
- [49] P. R. Vlachas, W. Byeon, Z. Y. Wan, T. P. Sapsis, and P. Koumoutsakos. Data-driven forecasting of high-dimensional chaotic systems with long short-term memory networks. *Proceedings of the Royal Society A: Mathematical, Physical and Engineering Sciences*, 474(2213):20170844, 2018.
- [50] E. Weinan. A proposal on machine learning via dynamical systems. *Communications in Mathematics and Statistics*, 1(5):1–11, 2017.
- [51] E. Weinan, C. Ma, and L. Wu. A comparative analysis of optimization and generalization properties of two-layer neural network and random feature models under gradient descent dynamics. *Sci. China Math*, 2019.
- [52] Y. Xie, B. Shi, H. Schaeffer, and R. Ward. SHRIMP: sparser random feature models via iterative magnitude pruning. *CoRR*, abs/2112.04002, 2021.
- [53] Z. Yang, Y. Bai, and S. Mei. Exact gap between generalization error and uniform convergence in random feature models. In *International Conference on Machine Learning*, pages 11704–11715. PMLR, 2021.
- [54] D. Zou, L. Wang, P. Xu, J. Chen, W. Zhang, and Q. Gu. Epidemic model guided machine learning for covid-19 forecasts in the united states. *MedRxiv*, 2020.

Appendix

Results on Simulated Data with 2% Noise

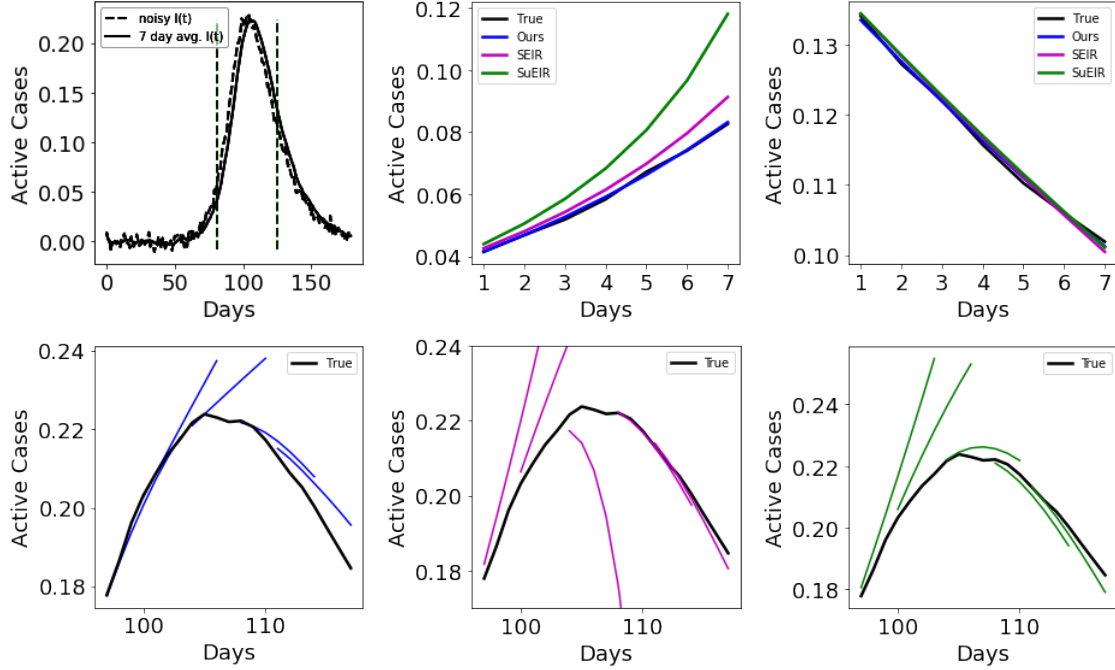


Figure 13: Results on simulated data with 2% noise added to input data. First row: Noisy training datasets from 0 upto 81^{st} and 125^{th} days out of 180 days (top left). The next two figures are the predicted values of the infectious variable $I(t)$ in the next seven days using SPADE4 (blue), SEIR model (magenta), and $S\mu EIR$ model (green) correspond to those two training datasets versus ground truth (black). Second row: Prediction of $I(t)$ for next seven days around the peak of the wave using SPADE4 (blue), SEIR model (magenta), and $S\mu EIR$ model (green) versus ground truth (black).